



Phenazine-based colorimetric and fluorometric probes for rapid recognizing of Hg²⁺ with high sensitivity and selectivity



Haitao Zhou^a, Lu Sun^b, Wei Chen^a, Guojian Tian^a, Yi Chen^a, Yiru Li^a, Jianhua Su^{a,*}

^aKey Laboratory for Advanced Materials and Institute of Fine Chemicals, East China University of Science & Technology, Shanghai 200237, PR China

^bInstitute of Modern Optics, Nankai University, Tianjin 300071, PR China

ARTICLE INFO

Article history:

Received 11 January 2016

Received in revised form 7 March 2016

Accepted 11 March 2016

Available online 12 March 2016

Keywords:

Phenazine

Colorimetric

Fluorometric

Probe

Hg²⁺

ABSTRACT

Two colorimetric and fluorometric probes, namely **2a** and **2b**, based on *N,N'*-disubstituted-dihydrophenazine analogues for rapid detection of Hg²⁺ with high sensitivity and selectivity were designed and synthesized by Heck coupling reaction. The responsive optical properties of the two sensors were investigated by UV–vis absorption and fluorescence spectroscopy in THF solution and **2a–b** were found to be exclusively responsive to Hg²⁺ rapidly. Remarkably, the detection limits of **2a–b** for Hg²⁺ were determined to be 4.8 and 2.6 nM, respectively. Moreover, the AIE and pH sensing properties of **2a–b** were investigated.

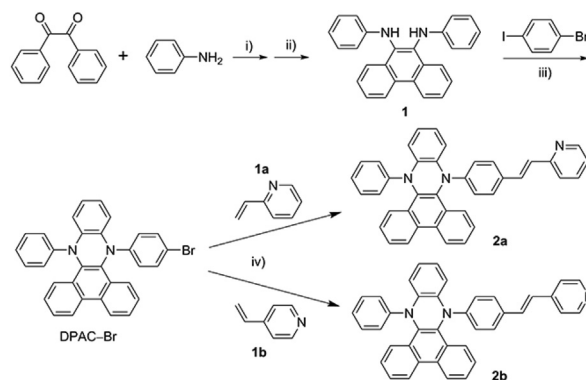
© 2016 Elsevier Ltd. All rights reserved.

1. Introduction

Mercury, as one of the most toxic heavy and transition metals (HTM), can be accumulated over time through the food chain¹ and cause serious damage to the brain, kidney, and nervous system of both human and animals,² and the US Environmental Protection Agency (EPA) has set the maximum permissible level of Hg²⁺ in drinking water at 2 ppb (10 nM).³ Thus exploring methods for detecting Hg²⁺ with high selectivity and sensitivity are of great importance. Compared with conventional techniques such as atomic absorption spectroscopy,⁴ coupled plasma mass spectroscopy,⁵ etc., which generally requiring expensive equipments and complicated operations,⁶ optochemical technology based on absorption or fluorescent detection takes advantages of simple detection procedures, high sensitivity, and with no requirement of expensive equipments.⁷ Therefore, tremendous efforts have been directed towards the design and synthesis of fluorescent probes for selective and sensitive detection of Hg²⁺.

Recently, pyridine-appended π -conjugated analogues with D-A structure involving the lone-pair electrons on the pyridine nitrogen atom have been widely used as HTM sensors, in which the pyridyl group(s) acts as the monodentate ligand(s) for metal ions.⁸ The phenazine-based derivative, 9,14-diphenyl-9,14-dihydrodibenzo

[*a,c*]phenazine (DPAC, see Scheme 1), possesses structure features of both triphenylamine and carbazole, which are widely employed in building optoelectronic materials.⁹ However, there are few reports on DPAC and its application as fluorescent probe for metal ions has not been reported to date. Herein, we present two novel probes **2a** and **2b** (Scheme 1) based on DPAC and pyridine for determining Hg²⁺ in THF solution. Pyridine can constitute π -conjugated D-A molecules when coupled with DPAC. The ethenyl was designed as linkage to modulate the communication between the



Scheme 1. Synthesis route of **2a–b**. Reagents and conditions: i) TiCl₄, toluene; ii) Li, MeOH; iii) Cu (CF₃SO₃)₂, K₂CO₃, trichlorobenzene, reflux; iv) Pd(OAc)₂, K₂CO₃, DMF, N₂, reflux.

* Corresponding author. Tel./fax: +86 21 6425 2288; e-mail address: bbsjh@ecust.edu.cn (J. Su).

pyridyl group and the DPAC core.¹⁰ Interestingly, remarkable changes were observed both in absorption and fluorescence spectra of **2a–b** when complexing with Hg^{2+} .

2. Results and discussion

2.1. Synthesis

The detailed synthetic route of **2a–b** was described in Scheme 1. The key intermediates, **1** and DPAC–Br, was synthesized according to previous literature.¹¹ Compounds **2a–b** were synthesized via Heck coupling reaction between DPAC–Br and **1a–b**, and confirmed by ^1H NMR, ^{13}C NMR and High-resolution mass spectroscopy (HRMS).

2.2. Solvatochromic effect

The solvatochromic effect is usually observed in compounds containing D–A pairs. Due to the presence of DPAC and pyridine, **2a** and **2b** possess typical D– π –A structure. To investigate the effect of solvent polarity on the optical properties of the probes, the emission spectra of **2a–b** in different solvents were recorded by increasing the polarity from dioxane to acetonitrile and the results are summarized in Fig. 1 and Fig. S1. As shown in Fig. S1, both the absorption spectra of **2a** and **2b** exhibited minor changes in various solvents. Meanwhile, as the polarity of the solvents increased, the emission peaks of **2a–b** gradually red shifted (**2a**: 428 nm–479 nm; **2b**: 425 nm–469 nm, from dioxane to acetonitrile) and accompanied by a broadening of the emission bands in polar solvents, indicating an intramolecular charge transfer (ICT) character in the excited state. To evaluate the solvatochromism of the two probes, the relationship between the solvent orientation polarizability (Δf) and the Stokes shift ($\Delta\nu$) was studied using the Lippert–Mataga equation (see Table S1).¹² The slopes of the fitting lines for **2a–b** were determined to be 7190 and 7390, respectively, according to the $\Delta\nu$ – Δf plots (Fig. S2).

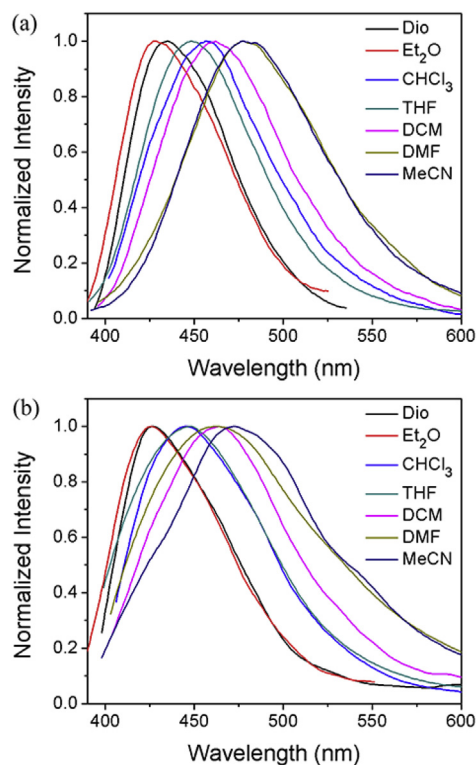


Fig. 1. Normalized fluorescence spectra of **2a** (a) and **2b** (b) in various solvents at concentration of 10 μM .

To investigate the relationship between the compounds' optical and charge transfer properties, three-dimensional geometries of **2a–b** were optimized using density functional theory (DFT) at the B3LYP/6-31G level of theory.¹³ Once the energies reached convergence, single point energies and molecular orbitals were subsequently computed with long-range corrected functionals cam-B3LYP and the diffused and polarized triple-zeta basis set 6-311+G*.¹⁴ Seen from Table S2, the HOMOs receive contribution from the styrylpyridine and piperazine moiety, while the LUMOs are mostly localized on the styrylpyridine and phenanthrene moiety. Upon photoexcitation, intramolecular charge transfer (ICT) is expected to occur in these two compounds. ICT effect could be facilitated in polar solvent and that's why the emission peaks of **2a–b** red shifted as the polarity of the solvent increased.

2.3. Aggregation induced enhanced emission properties

The optical properties of **2a** and **2b** were investigated in THF/water (from 10:0 to 1:9) mixtures and the results are shown in Fig. 2. It could be seen that both **2a** and **2b** showed very weak fluorescence in pure THF. The photoluminescence (PL) intensity of **2a** was slightly quenched when the water content was 10% and stayed almost constant when water ratio below 80%. Noticeably, when the water content increased from 80% to 90%, the PL intensity boosted to the maximum with a 22-fold increase. In addition, the emission maxima of **2a** had a red shift of about 20 nm when the water fraction increased from 0% to 90%, which could be ascribed to the increasing accumulation of the molecules by aggregation. Similar phenomenon was observed for **2b**. It kept emitting weakly when the water fraction increased from 0% to 80% and the PL intensity reached maximum when water was added up to 90%, which is nearly 20 times stronger than that in pure THF solution. Therefore, both **2a** and **2b** are AIEE active.¹⁵ What's more, the absorption spectra of **2a–b** in THF solution and in THF/water mixture were observed (Fig. S3). It can be seen that the latter were slightly red-shifted, which was caused by nano-aggregation.

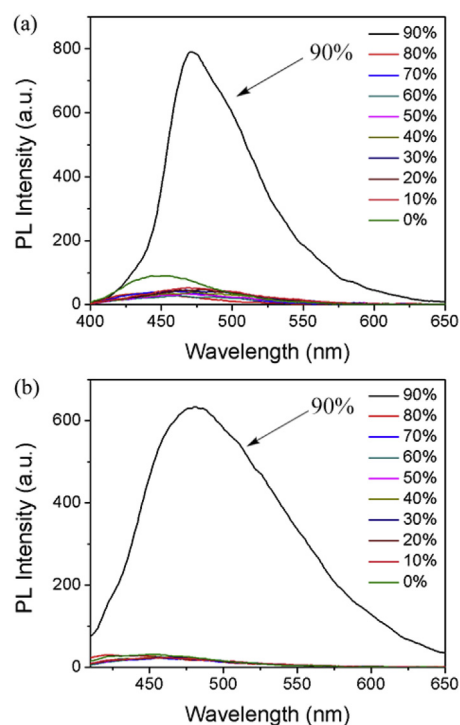


Fig. 2. Photoluminescence spectra of **2a** (a) and **2b** (b), respectively, in THF/water mixtures.

The AIE nature of **2a–b** could be further clarified by the optimized geometries. It can be seen from Table S2 that both **2a–b** present highly twisted saddle-shaped configurations with two rotatable phenyls, which are favorable for nonradiative decay in solution. When aggregated, not only the intramolecular rotations are hindered, but also the formation of π – π stacking is prevented, making the aggregates emit intensely.

2.4. pH sensing

Due to the presence of pyridyl group, **2a** and **2b** possess protonation and deprotonation process. Thus, the spectroscopic properties of the two probes were studied in phosphate buffer solutions (PBS) in a pH range from 2.20 to 10.04, and the results are illustrated in Fig. 3. Below pH 3.08, **2a** showed very weak fluorescence, which could be ascribed to the protonated **2a**. Increasing the pH value gives rise to higher fluorescence intensity at 467 nm, which could be caused by aggregation of deprotonated **2a** in water. The situation was similar for **2b**. It emitted weakly and remained almost constant when pH below 4.04, and its PL intensity was gradually enhanced along with the further increase of pH value. Therefore, both **2a–b** could act as pH probes.

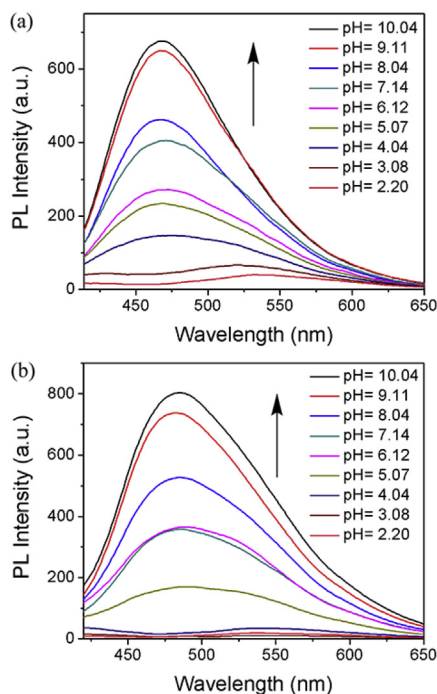


Fig. 3. Fluorescence spectra of **2a** (a) and **2b** (b) in aqueous solution as a function of pH. Concentration: 10 μ M. Excitation wavelength is 380 nm for **2a** and 385 nm for **2b**.

2.5. Optical response to various metal ions

The sensing behaviors of **2a–b** were first studied by UV–Visible absorption measurements in THF/water mixtures. However, **2a–b** couldn't respond to any metal ion in various THF/water mixtures but could selectively respond to Hg^{2+} in pure THF. It was found that both free **2a–b** in THF were achromatous and showed absorption maximum at around 360 nm. Absorption responses of **2a–b** were carried out upon addition of 1.0 equiv of various metal ions (Ag^+ , Ca^{2+} , Co^{2+} , Cr^{3+} , Cu^{2+} , Fe^{2+} , Fe^{3+} , Hg^{2+} , Mg^{2+} , Mn^{2+} , Ni^{2+} , Pb^{2+} and Zn^{2+}) in aqueous solution. It could be seen from Fig. 4 and Fig. S5 that both **2a** and **2b** exhibit a remarkably distinctive spectroscopic response toward addition of Hg^{2+} , resulting in the decrease of absorbance at ca. 360 nm and a new absorption peak at ca.

430 nm accompanied by the color of the solution turning from colorless to yellow, which could be observed by the naked eye (Fig. S4). Meanwhile, no significant changes were observed in the parallel experiments with other metal ions. Fig. 4b showed the absorbance ratios of the peak at 425 nm and 360 nm (A_{425}/A_{360}) in the presence of various metal ions. It is clear that for **2a** solution A_{425}/A_{360} showed little increase upon addition of various metal ions except for Hg^{2+} . Similar properties were observed in **2b** solution (Fig. S5).

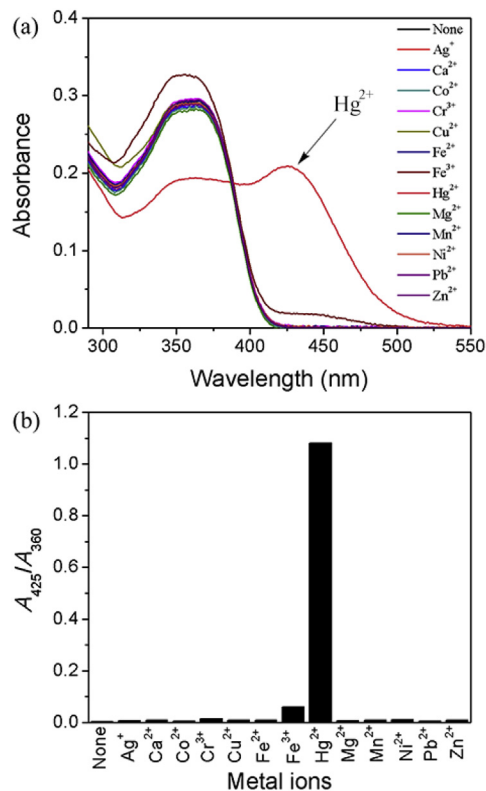


Fig. 4. (a) Absorption spectra of **2a** in THF solution containing different metal ions (1.0 equiv) at same concentration (10 μ M); (b) Absorption intensity ratio (A_{425}/A_{360}) of **2a** (10 μ M) versus different metal ions.

Subsequently, fluorescence responses of **2a** and **2b** over various metal ions have been tested, and the results are illustrated in Fig. 5. In the absence of any ions, both **2a** and **2b** showed an emission in THF. The addition of Hg^{2+} (1.0 equiv) caused the quenching of the fluorescence of **2a–b**. In contrast, there was no significant fluorescence change observed in **2a–b** solutions in the presence of 10.0 equiv other metal ions. Significantly, both **2a** and **2b** could bind to Hg^{2+} within several seconds and the complexes could remain stable for several days. These evidence suggest **2a–b** possess good selectivity towards Hg^{2+} and could be applied in rapid detection of Hg^{2+} . Thus Hg^{2+} titration of **2a–b** by absorption and fluorescence spectroscopy methods were carried out.

We then explored the optical response of **2a** by monitoring the changes in the absorption and fluorescence spectra in THF with continuous addition of aqueous Hg^{2+} . Upon addition of 0–1.5 equiv of Hg^{2+} , the absorbance at 360 nm decreased gradually, accompanied by the enhancement of a new absorption band at 425 nm, and with an isosbestic point at 388 nm (Fig. 6a), suggesting the formation of a complex between the probe and Hg^{2+} . It happened that the absorption spectrum of **2a** became constant after adding 1.5 equiv of Hg^{2+} . As for the fluorescence spectrum of **2a**, it exhibited noticeable fluorescence quenching caused by spin-orbit

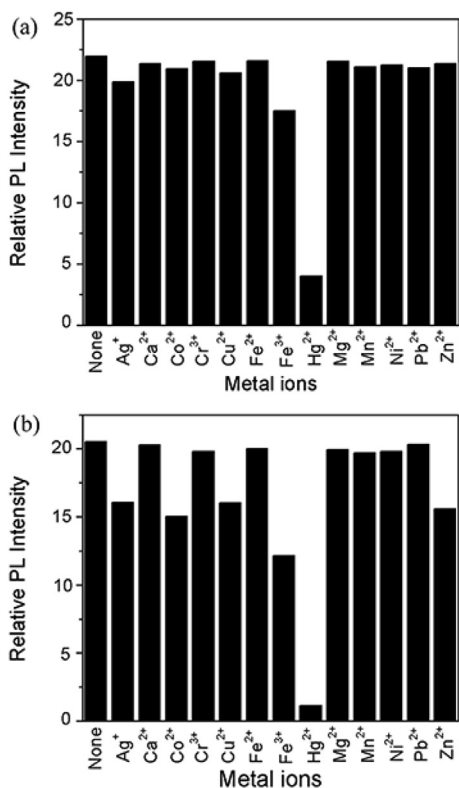


Fig. 5. (a) Fluorescence intensities at 450 nm of **2a** (10 μ M) in THF in the presence of various ions (1.0 equiv for Hg^{2+} and 10.0 equiv for other ions, $\lambda_{\text{ex}}=360$ nm); (b) Maximum fluorescence intensities of **2b** (10 μ M) in THF in the presence of various ions (1.0 equiv for Hg^{2+} and 10.0 equiv for other ions, $\lambda_{\text{ex}}=366$ nm).

coupling or electron transfer¹⁶ upon progressively addition of Hg^{2+} and reached saturation point when Hg^{2+} concentration was 1.5 equiv, which is in line with the tendency observed in absorption studies (Fig. 6b).

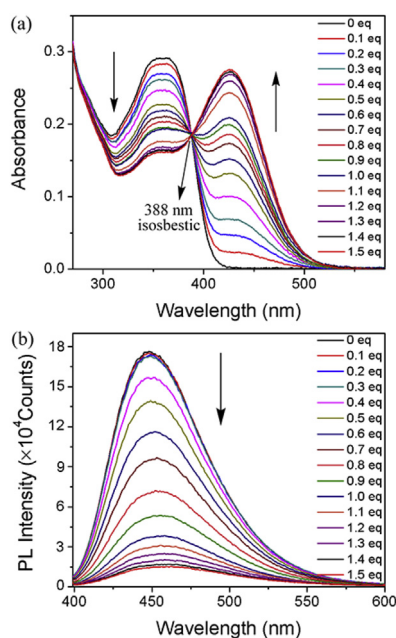


Fig. 6. Absorption (a) and fluorescence (b) spectra of **2a** in THF (10 μ M) upon addition of 0–1.5 equiv of aqueous Hg^{2+} ; $\lambda_{\text{ex}}=388$ nm.

Similarly, probe **2b** showed main absorption band centering at 366 nm, and it also decreased gradually as Hg^{2+} was added, accompanied by a new rise at 432 nm (Fig. 7a). The absorption spectrum of **2b** remained unchanged after adding more than 1.5 equiv of Hg^{2+} . Interestingly, **2b** exhibited weakened emission spectra and red shifted from 450 to 520 nm when Hg^{2+} was added (Fig. 7b). Notably, the detection limits of **2a–b** for Hg^{2+} were determined by the absorption spectroscopy measurements (see Fig. S6) to be 4.8 and 2.6 nM, respectively, which is much lower than 10 nM, the maximum contaminant limit defined by the US EPA for drinking water. Additionally, the detection limits of **2a–b** were also calculated by the fluorescence spectroscopy measurements (see Fig. S7).

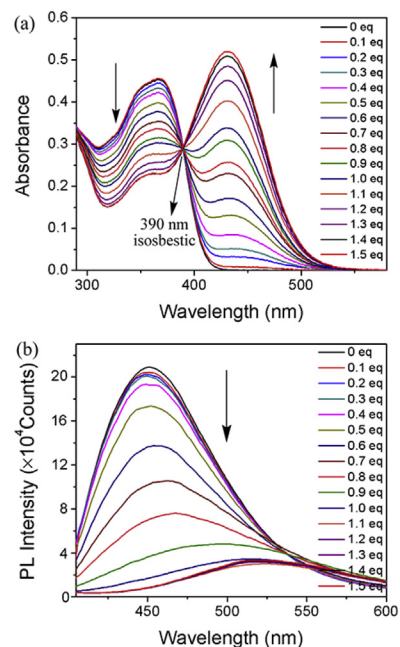


Fig. 7. Absorption (a) and fluorescence (b) spectra of **2b** in THF (10 μ M) upon addition of 0–1.5 equiv of aqueous Hg^{2+} ; $\lambda_{\text{ex}}=390$ nm.

2.6. Mechanism studies

^1H NMR titration spectra were studied to make certain of the coordination mechanism of **2a–2b** with Hg^{2+} . Fig. 8 presents the ^1H NMR spectra of **2a** in $\text{DMSO}-d_6$ in the presence of different equivalent of Hg^{2+} . After carefully comparing the ^1H NMR titration spectra of **2a** in the presence and absence of Hg^{2+} , we found that the chemical shifts of the resonances associated with the pyridyl protons (H_1 , H_2 , H_3 and H_4) and the ethenyl protons (H_5 and H_6) showed significant changes upon complexation with Hg^{2+} , while the chemical shifts of the protons in DPAC moiety just displayed negligible changes. These observations revealed that Hg^{2+} has coordinated with pyridine moiety. What's more, the spectrum remained unchanged after adding 0.5 equiv of Hg^{2+} , suggesting the 2:1 stoichiometry of the complexes between **2a** and Hg^{2+} . The 2:1 stoichiometry between **2a** and Hg^{2+} was then supported by the MALDI-TOF MS spectrum (Fig. S9a) in which the labeled signal at m/z 638.18 (calcd for $\text{C}_{78}\text{H}_{54}\text{HgN}_6$, 638.21) was assigned to $[\text{2a} \cdot \text{Hg}^{2+} \cdot \text{2a}]^{2+}$ ion. Moreover, the result of Job's plot analysis further confirmed the 2:1 stoichiometry (Fig. S10a). Similar changes were observed in the ^1H NMR titration spectra of **2b** (Fig. S8) and the 2:1 stoichiometry between **2b** and Hg^{2+} was also fully validated by the MALDI-TOF MS (Fig. S9b) and the Job's plot analysis (Fig. S10b).

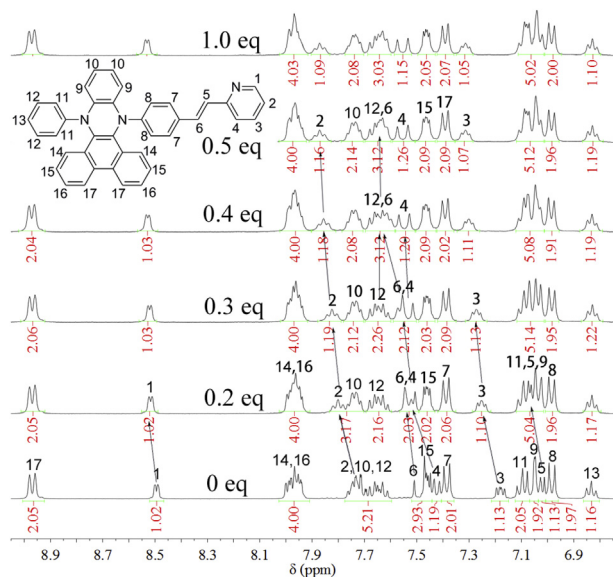


Fig. 8. Partial ^1H NMR spectra of **2a** in $\text{DMSO}-d_6$ with increasing concentration of Hg^{2+} .

2.7. Electrochemical properties

The electrochemical properties of **2a–2b** were investigated by cyclic voltammetry (CV). Pertinent data are listed in Table 1. The CV of **2a–2b** was measured in THF solution with 0.1 M *n*-Bu₄NPF₆ as supporting electrolyte, with an SCE reference electrode, platinum-button working electrodes, and a platinum-wire counter electrode, as shown in Fig. 9. Both the onset oxidation potentials of **2a–2b** are 0.74 V according to the CV curve. Thus, the HOMO values for **2a–2b** are both -5.54 eV, derived from the onset oxidation potentials given above. The LUMO values of **2a–2b** can be determined from

Table 1
Electrochemical and optical properties of **2a–2b**^a

	$E_{\text{onset-ox}}$ (V)	HOMO (eV)	λ_{onset} (nm)	E_g (eV)	LUMO (eV)
2a	0.74	-5.54	415	2.99	-2.55
2b	0.74	-5.54	420	2.95	-2.59

^a Abbreviation: $E_{\text{onset-ox}}$ (onset oxidation potential) was measured versus ferrocene, $\text{HOMO} = -(E_{\text{onset-ox}} - E_{1/2}(\text{ferrocene}) + 4.8)$ eV, $\lambda_{\text{onset}} = \text{onset absorption wavelength}$, $E_g = \text{energy band gap determined from } \lambda_{\text{onset}}$, $\text{LUMO} = E_g + \text{HOMO}$.

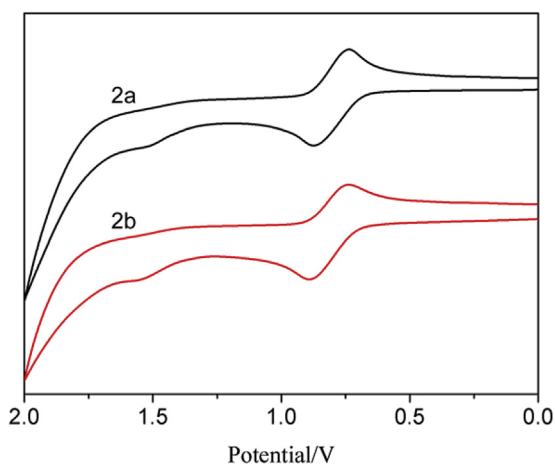


Fig. 9. Cyclic voltammograms of **2a–2b** in THF solution with 0.1 M of tetrabutylammonium hexafluorophosphate (*n*-Bu₄NPF₆).

their band gaps and HOMO levels to be -2.55 and -2.59 eV, respectively.

3. Conclusion

In summary, we've presented the synthesis and properties of two phenazine-based probes, **2a–b**, for rapid recognizing of Hg^{2+} with high selectivity and sensitivity in THF. Both the sensors exhibited a gradual diminution at their original maximum wavelength accompanied by an enhancement at a longer wavelength, and the color changes from achromatous to yellow upon addition of Hg^{2+} , thus could serve as naked eye probes. Meanwhile, **2a** and **2b** displayed a progressively decrease in fluorescence intensity upon addition of Hg^{2+} , therefore **2a–b** could detect quantitative Hg^{2+} by both absorption and fluorescence spectroscopy methods. Notably, the detection limit of **2a–b** was determined to be 4.8 and 2.6 nM, respectively, by the absorption spectroscopy method. It's mentionable that both **2a** and **2b** could rapidly response to Hg^{2+} in several seconds. In addition, **2a–b** showed AIE effect in THF/water mixtures and could act as pH probes. These properties can promote DPAC as promising building block for constructing Hg^{2+} probes with high performance.

4. Experimental section

4.1. Materials

1a and **1b** were purchased from Energy Chemical Reagent Co., Ltd. The salts used in stock solutions of metal ions were AgNO_3 , CaCl_2 , $\text{CoCl}_2 \cdot 6\text{H}_2\text{O}$, $\text{CrCl}_3 \cdot 6\text{H}_2\text{O}$, $\text{CuCl}_2 \cdot 2\text{H}_2\text{O}$, $\text{FeSO}_4 \cdot 7\text{H}_2\text{O}$, $\text{FeCl}_3 \cdot 6\text{H}_2\text{O}$, $\text{Hg}(\text{ClO}_4)_2 \cdot 3\text{H}_2\text{O}$, $\text{MgCl}_2 \cdot 6\text{H}_2\text{O}$, $\text{MnCl}_2 \cdot 4\text{H}_2\text{O}$, $\text{NiSO}_4 \cdot 6\text{H}_2\text{O}$, PbCl_2 , ZnCl_2 . All of them were of analytical reagent grade and used without purification. Water used in experiment was double distilled water. THF was pre-dried over sodium for 24 h and then redistilled under argon atmosphere with sodium prior to use.

4.2. Instruments

^1H and ^{13}C NMR spectra were measured on Bruker AM-400 spectrometer using $\text{DMSO}-d_6$ as solvent and tetramethylsilane (TMS, $\delta=0$ ppm) as internal standard. Mass spectra were recorded on Waters LCT Premier XE spectrometer. MS of complexes formed by **2a/2b** with Hg^{2+} were measured on an AB Sciex 4800 plus Matrix-Assisted Laser Desorption Ionization Time of Flight (MALDI-TOF) mass spectrometer. The UV/Vis spectra were recorded on Nicolet CARY 100 spectrophotometer. The PL spectra were taken on Varian-Cary fluorescence spectrophotometer or Horiba Fluoromax 4. The pH values between 2.20 and 10.04 were measured by PHSJ-4A pH meter. The quantum yield for solid powders was measured by Quanta-w F-3029 Integrating Sphere.

4.3. Synthesis

4.3.1. *N*₉,*N*₁₀-Diphenylphenanthrene-9,10-diamine (**1**). 1 mL TiCl_4 was dropwise added through an injector to a cooled solution (0°C) of benzil (5.0 g, 23.8 mmol) and aniline (5.4 mL, 59.5 mmol) in toluene (70 mL). The solution was stirred at rt for 12 h. The reactant was isolated with solvent under reduced pressure and dissolved in 100 mL THF. Lithium silk (0.41 g, 59.5 mmol) was added in portion at rt and refluxed for 8 h. Methanol was added dropwise to the filtrate with continued stirring until the evolution of hydrogen ceased. Then water was added, and the product was extracted with DCM. After drying with MgSO_4 and removal of DCM, the resulting precipitate was refluxed in ethanol, filtrated, washed with ethanol and dried under vacuum to give a pale yellow solid (6.1 g). Yield: 71.2%. ^1H NMR ($\text{DMSO}-d_6$, 400 MHz, TMS), δ : 8.88 (d, $J=8.0$ Hz, 2H), 7.93 (d, $J=8.0$ Hz,

2H), 7.68 (s, 2H), 7.65 (t, $J=8.0$ Hz, 2H), 7.55 (7, $J=7.6$ Hz, 2H), 7.00 (t, $J=8.0$ Hz, 4H), 6.60 (t, $J=7.2$ Hz, 2H), 6.52 (d, $J=7.6$ Hz, 4H).

4.3.2. 9-(4-Methoxyphenyl)-14-phenyl-9,14-dihydrodibenzo[*a,c*]phenazine (DPAC-Br). In a 100 mL three-neck flask, 5.0 g (13.87 mmol) N_9,N_{10} -diphenylphenanthrene-9,10-diamine, 3.9 g (13.87 mmol) bromo-4-iodobenzene, 2.5 g (18.09 mmol) K_2CO_3 , 1.25 g (3.45 mmol) $Cu(CF_3SO_3)_2$, 10.0 g trichlorobenzene was added. The mixture stirred for 8 h under refluxed. The trichlorobenzene was taken out by vacuum distillation. After cooling, added 50 mL DCM and stirred for 20 min, filtered the mixture. The combined organic layer was purified by column chromatography on silica (PE:DCM=10:1 v/v) to give a light yellow solid (2.5 g). Yield: 35.1%. 1H NMR (DMSO- d_6 , 400 MHz, TMS), δ : 8.95 (d, $J=8.4$ Hz, 2H), 7.93–7.98 (m, 3H), 7.88–7.91 (m, 1H), 7.59–7.76 (m, 4H), 7.43–7.46 (m, 2H), 7.22 (d, $J=9.2$ Hz, 2H), 7.07–7.12 (m, 2H), 7.01 (d, $J=7.6$ Hz, 2H), 6.82–6.91 (m, 3H). HRMS (m/z): M calcd for: $C_{32}H_{21}BrN_2$, 512.0888, found: 512.0889.

4.3.3. (E)-9-Phenyl-14-(4-(2-(pyridin-2-yl)vinyl)phenyl)-9,14-dihydrodibenzo[*a,c*]phenazine (2a). In a round-bottom flask, DPAC-Br (0.2 g, 0.39 mmol), **1a** (82 mg, 0.78 mmol) and potassium carbonate (65 mg, 0.47 mmol) were dissolved in 30 mL DMF, and catalytic amount of palladium acetate was added, then the mixture was refluxed under N_2 atmosphere for 18 h. Upon cooling, DMF was removed under reduced pressure, the residue was dissolved in CH_2Cl_2 , washed with water, dried over anhydrous $MgSO_4$ and concentrated using a rotary evaporator. The residue was purified by column chromatography on silica (PE/ CH_2Cl_2 =1:3 v/v) to give a pale yellow solid (0.1 g). Yield: 47.7%. Melting point: 256–258 °C. FTIR (KBr, cm^{-1}): 3058.0 (v, =C–H), 1589.1, 1496.5 (v, Ar–C=C), 1337.2 (Ar–C–N). 1H NMR (DMSO- d_6 , 400 MHz, TMS), δ : 8.97 (d, $J=8.0$ Hz, 2H), 8.50 (d, $J=4.0$ Hz, 1H), 8.00–7.94 (m, 4H), 7.76–7.61 (m, 5H), 7.51–7.37 (m, 6H), 7.20–7.16 (m, 1H), 7.12–6.98 (m, 7H), 6.85–6.82 (m, 1H). ^{13}C NMR (DMSO- d_6 , 100 MHz), δ : 155.25, 149.41, 149.32, 147.05, 147.03, 144.12, 143.43, 137.32, 136.68, 131.41, 129.59, 129.44, 129.31, 129.04, 128.27, 128.21, 127.92, 127.45, 127.36, 127.24, 127.08, 127.04, 126.00, 125.82, 125.74, 123.86, 123.83, 123.75, 121.89, 121.61, 117.14, 116.36. HRMS (m/z): $[M+H]^+$ calcd for: $C_{39}H_{28}N_3$, 538.2283, found: 538.2279.

4.3.4. (E)-9-Phenyl-14-(4-(2-(pyridin-4-yl)vinyl)phenyl)-9,14-dihydrodibenzo[*a,c*]phenazine (2b). Probe **2b** was synthesized by the same procedure as described above for **2a** using compound **1** and compound **1b**. Yield: 55.2%. Melting point: 180–182 °C. FTIR (KBr, cm^{-1}): 3068.9 (v, =C–H), 1594.9, 1496.5 (v, Ar–C=C), 1340.3 (Ar–C–N). 1H NMR (DMSO- d_6 , 400 MHz, TMS), δ : 8.95 (d, $J=12.0$ Hz, 2H), 8.46 (d, $J=8.0$ Hz, 2H), 7.99–7.92 (m, 4H), 7.75–7.70 (m, 2H), 7.63 (dd, $J=8.0, 12.0$ Hz, 2H), 7.47–7.41 (m, 4H), 7.37–7.32 (m, 3H), 7.10–6.92 (m, 7H), 6.82 (m, 1H). ^{13}C NMR (DMSO- d_6 , 100 MHz), δ : 149.86, 147.20, 147.00, 144.48, 144.14, 143.36, 137.37, 136.62, 132.35, 129.56, 129.40, 128.99, 128.23,

128.13, 127.93, 127.39, 137.32, 132.23, 127.06, 127.05, 127.00, 126.01, 125.72, 123.83, 123.74, 123.70, 123.68, 123.47, 121.57, 120.48, 117.10, 116.23. HRMS (m/z): $[M+H]^+$ calcd for: $C_{39}H_{28}N_3$, 538.2283, found: 538.2288.

Acknowledgements

This work was supported by National Natural Science Foundation of China (20772031), the National Basic Research 973 Program (2006CB806200), the Fundamental Research Funds for the Central Universities (WJ0913001), and the Scientific Committee of Shanghai (10520709700).

Supplementary data

Supplementary data (The characterization (NMR and HRMS) and computational analysis data of **2a–b** are available) associated with this article can be found in the online version, at <http://dx.doi.org/10.1016/j.tet.2016.03.036>.

References and notes

- de Silva, A. P.; Fox, D. B.; Huxley, A. J. M.; Moody, T. S. *Coord. Chem. Rev.* **2000**, *205*, 41–57.
- (a) Boening, D. W. *Chemosphere* **2000**, *40*, 1335–1351; (b) Benoit, J. M.; Fitzgerald, W. F.; Damman, A. W. *Environ. Res.* **1998**, *78*, 118–133; (c) Gutknecht, J. J. *Membr. Biol.* **1981**, *61*, 61–66.
- EPA Fact Sheet EPA-823-F-01–001Mercury Update: Impact on Fish Advisories; Environmental Protection Agency, Office of Water: Washington, DC, 2001.
- Zheng, C.; Li, Y.; He, Y.; Ma, Q.; Hou, X. J. *Anal. At. Spectrom.* **2005**, *20*, 746–750.
- Beauchemin, D. *Anal. Chem.* **2008**, *80*, 4455–4486.
- Quang, D. T.; Kim, J. S. *Chem. Rev.* **2010**, *110*, 6280–6301.
- (a) Sarkar, M.; Banthia, S.; Samanta, A. *Tetrahedron Lett.* **2006**, *47*, 7575–7578; (b) Cheung, S. M.; Chan, W. H. *Tetrahedron* **2006**, *62*, 8379–8383.
- (a) Xue, H.; Tang, X. J.; Wu, L. Z.; Zhang, L. P.; Tung, C. H. *J. Org. Chem.* **2005**, *70*, 9727–9734; (b) Brombosz, S. M.; Zuccherro, A. J.; Phillips, R. L.; Vazquez, D.; Wilson, A.; Bunz, U. H. F. *Org. Lett.* **2007**, *9*, 4519–4522; (c) Feng, X. J.; Tian, P. Z.; Xu, Z.; Chen, S. F.; Wong, M. S. J. *Org. Chem.* **2013**, *78*, 11318–11325.
- (a) Wang, B.; Wang, Y. C.; Hua, J. L.; Jiang, Y. H.; Huang, J. H.; Qian, S. X.; Tian, H. *Chem.—Eur. J.* **2011**, *17*, 2647–2655; (b) Jiang, Y. H.; Wang, Y. C.; Hua, J. L.; Tang, J.; Li, B.; Qian, S. X.; Tian, H. *Chem. Commun.* **2010**, *46*, 4689–4691; (c) Huang, W.; Tang, F. S.; Li, B.; Su, J. H.; Tian, H. *J. Mater. Chem. C* **2014**, *2*, 1141–1148.
- Xue, H.; Tang, X. J.; Wu, L. Z.; Tung, C. H. *J. Org. Chem.* **2005**, *70*, 9727–9734.
- (a) Su, J. H.; Shen, L. P.; Zhao, D. M.; Zhang, Z. Y.; Wang, T. H.; Han, J. L.; Tian, H. *Faming Zhuanli Shenqing* **2012** CN 102491950 A 20120613; (b) Ullah, F.; Kindermann, M. K.; Jones, P. G.; Heinicke, J. *Organometallics* **2009**, *28*, 2441–2449.
- Mataga, N.; Kaifu, Y.; Koizumi, M. *Bull. Chem. Soc. Jpn.* **1956**, *29*, 465–470.
- (a) Becke, A. D. *J. Chem. Phys.* **1993**, *98*, 5648–5642; (b) Lee, C.; Yang, W. T.; Parr, R. G. *Phys. Rev. B* **1988**, *37*, 785–789; (c) Petersson, G. A.; Bennett, A.; Tensfeldt, T. G.; Al-Laham, M. A.; Shirley, W. A.; Mantzaris, J. *J. Chem. Phys.* **1988**, *89*, 2193–2218.
- (a) Yanai, T.; Tew, D. P.; Handy, N. C. *Chem. Phys. Lett.* **2004**, *393*, 51–57; (b) McLean, A. D.; Chandler, G. S. *J. Chem. Phys.* **1980**, *72*, 5639–5648.
- (a) Hong, Y. N.; Lam, J. W. Y.; Tang, B. Z. *Chem. Commun.* **2009**, 4332–4353; (b) Hong, Y. N.; Lam, J. W. Y.; Tang, B. Z. *Chem. Soc. Rev.* **2011**, *40*, 5361–5388; (c) Mei, J.; Hong, Y. N.; Lam, J. W. Y.; Qin, A. J.; Tang, Y. H.; Tang, B. Z. *Adv. Mater.* **2014**, *26*, 5429–5479; (d) Mei, J.; Leung, N. L. C.; Kwok, R. T. K.; Lam, J. W. Y.; Tang, B. Z. *Chem. Rev.* **2015**, *115*, 11718–11940.
- (a) McClure, D. S. *J. Chem. Phys.* **1952**, *20*, 682–686; (b) Yu, M. X.; Shi, M.; Chen, Z. G.; Li, F. Y.; Li, X. X.; Gao, Y. H.; Xu, J.; Yang, H.; Zhou, Z. G.; Yi, T.; Huang, C. *Chem.—Eur. J.* **2008**, *14*, 6892–6900; (c) Li, G. K.; Xu, Z. X.; Chen, C. F.; Huang, Z. T. *Chem. Commun.* **2008**, *15*, 1774–1776.